

Learning the Intrinsic Dimensionality of Fermi-Pasta-Ulam-Tsingou Trajectories: A Nonlinear Approach using a Deep Autoencoder Model

Gionni Marchetti *

(Dated: January 28, 2026)

We address the intrinsic dimensionality (ID) of high-dimensional trajectories, comprising $n_s = 4\,000\,000$ data points, of the Fermi-Pasta-Ulam-Tsingou (FPUT) β model with $N = 32$ oscillators. To this end, a deep autoencoder (DAE) model is employed to infer the ID in the weakly nonlinear regime ($\beta \lesssim 1$). We find that the trajectories lie on a nonlinear manifold of dimension $m^* = 2$ embedded in a 64-dimensional phase space. The DAE further reveals that this dimensionality increases to $m^* = 3$ at $\beta = 1.1$, coinciding with a symmetry breaking transition, in which additional energy modes with even wave numbers $k = 2, 4$ become excited. Finally, we discuss the limitations of the linear approach based on principal component analysis (PCA), which fails to capture the underlying structure of the data and therefore yields unreliable results in most cases.

I. INTRODUCTION

Fermi believed that weakly coupled nonlinear systems would inevitably exhibit ergodic behavior, as required for approaching thermal equilibrium [1]. As a consequence, in 1953, the first computer simulations of the Fermi-Pasta-Ulam-Tsingou (FPUT) model, a one-dimensional chain of weakly nonlinearly coupled oscillators, started aiming to study the system's thermalization, which in turn should have confirmed the validity of *ergodic hypothesis* [2–7]. In contrast, the energy recurrence phenomenon observed from simulations, for which the total energy was shared between a few energy modes only, seemed to contradict the ergodic hypothesis, a fact often referred to as the FPUT paradox.

Since then, the FPUT model has had a huge impact on our understanding of nonlinear dynamics and deterministic chaos. It would be an impossible task to mention all the important contributions made in the last seventy years, attempting to explain the peculiar dynamical features of FPUT chain. Here, we limit ourselves to recall that it was found that the recurrence phenomenon can be linked to Kolmogorov-Arnol'd-Moser (KAM) theorem [8–10], Toda lattice [11, 12], the solitonic behaviour of Korteweg de Vries (KdV) equation [13] and q-breathers [14, 15]. On the other hand, there exist various theories and methods attempting to explain how eventually the system approaches the equilibrium: existence of a stochastic threshold [16, 17], the FPUT metastability [5, 18, 19], and the spectral-entropy equipartition indicator [5, 20].

Recently, a data-driven approach based on principal component analysis (PCA) was proposed to infer the intrinsic (or effective) dimensionality (ID) m^* of the high-dimensional trajectories of the FPUT β model with $N = 32$ oscillators [21]. This work was chiefly motivated by the observation that the ergodic hypothesis requires trajectories to lie on a constant-energy hypersurface of dimension $n - 1$ in \mathbb{R}^n ($n = 2N$) [22]. As a result, thermal equilibrium cannot be reached when the trajectories lie on

very low-dimensional manifolds, a scenario which aligns with the application of KAM theorem to FPUT model, in a weakly nonlinear regime [23]. In fact, accordingly to KAM theorem the orbits should be constrained to low-dimensional invariant tori [24, 25]. In this regard, PCA when applied to entire trajectory data consisting of $n_s = 4\,000\,000$ data points, with the initial condition corresponding to excitation of only the first energy mode ($k = 1$), estimates the ID to be either 2 or 3 when $\beta \lesssim 1.1$. These findings strongly suggest a non-ergodic behavior, and are consistent with other qualitative observations that support the underlying quasi-periodic motion of FPUT system: the hexagonal patterns shown by Poincaré maps [26], and the energy recurrences observed from the simulations [21].

However, being linear, PCA provides a rather limited approach to the problem at hand [27–32]. Indeed, it assumes that the data points lie on optimal hyperplanes of a given rank m (or equivalently, on m -dimensional linear subspaces if data is centered), which is not necessarily the case, as shown by a qualitative analysis of early-stage orbits, performed using t -distributed stochastic neighbor embedding (t -SNE), a nonlinear manifold learning algorithm [21, 33–36]. More importantly, the inherent limitation of a linear approach was further confirmed by the analysis of trajectory data for $\beta = 0.1$, provided by the multi-chart flows, a Riemannian manifold learning method [37]. Specifically, this state-of-the-art method suggests that the trajectory lies near a nonlinear Riemannian manifold of dimension $m^* = 2$. Curiously, in such a case Participation Ratio (PR) heuristic [38] (Eq. B5), applied to the PCA eigenvalues, yields the very same result, but only accidentally: in fact, PCA would be expected to overestimate the intrinsic dimensionality by one, thus predicting $m^* = 3$ [39] (see Sect. IV).

Accordingly, in this work, we shall replace the PCA with its nonlinear generalization: the autoencoder (AE) [40, 41]. The AE is a type of artificial neural network (ANN), capable of learning the nonlinear structure of the data. In particular, we shall employ a relatively simple undercomplete deep autoencoder (DAE) model for learning the nonlinear structure of trajectory data (see Sect. III). We found

* gionniamarchetti@gmail.com

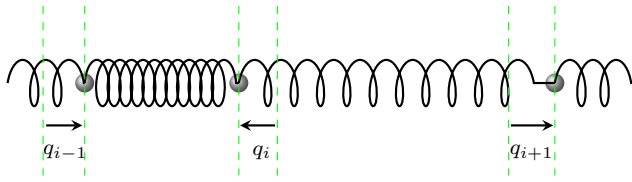


FIG. 1. The FPUT chain consists in a discrete system of equal mass points connected by springs. The coordinate q_i represents the displacement of i -th point from equilibrium.

that this model can learn and generalizes appropriately, yielding negligible reconstruction errors in comparison to those obtained using PCA. From the DAE reconstruction error curves, the corresponding elbow points estimate $m^* = 2$ for all available trajectory data associated with the recurrence phenomenon $\beta \lesssim 1$ (see Fig. 4).

Furthermore, the DAE model predicts that the intrinsic dimensionality increases by unity, i.e., $m^* = 3$, when $\beta = 1.1$. We find that this change is associated with the onset of a symmetry breaking (SB) phenomenon characteristic of the β model, whereby additional energy modes with even wave numbers, $k = 2, 4$, begin to share the systems total energy. In contrast to the DAE model, this important variation in the ID is completely missed by principal component analysis, for which the estimated ID remains constant as $\beta \rightarrow 1.1$, regardless of the suitable heuristic employed, such as Kneedle algorithm (KA) [42], PR or Kaiser criterion (KC) [43], to estimate it.

II. FPUT β MODEL

The FPUT model describes a one-dimensional chain of N nonlinear oscillators whose spring constants and masses are set to unity (see Fig. 1). In particular, the β ($\beta > 0$) model has the following Hamiltonian $H(q, p)$ where $q = (q_1, \dots, q_N)$ and $p = (p_1, \dots, p_N)$ [44]

$$H(q, p) = \frac{1}{2} \sum_{i=1}^N p_i^2 + \frac{1}{2} \sum_{i=0}^N (q_{i+1} - q_i)^2 + \frac{\beta}{4} \sum_{i=0}^N (q_{i+1} - q_i)^4. \quad (1)$$

Accordingly, the β model's equations of motion are the following [45]

$$\begin{cases} \dot{q}_i = p_i, \\ \dot{p}_i = q_{i+1} + q_{i-1} - 2q_i + \beta[(q_{i+1} - q_i)^3 - (q_i - q_{i-1})^3]. \end{cases} \quad (2)$$

Note that in Eq. 2 the index i runs from 0 to $N + 1$. This is why we assume that the chain has fixed ends, i.e.,

$q_0 = q_{N+1} = 0$, and hence $p_0 = p_{N+1} = 0$ (Dirichlet boundary conditions).

From a mathematical point of view, the Cauchy problem for the first-order system in Eq. 2 is well posed; that is, the solution exists and is unique because the vector field is analytic, being polynomial, as the number of oscillators N is finite [46]. However, the solution can be obtained only through numerical integration. To this end, we employed the velocity Störmer-Verlet scheme, which is a second-order symplectic integrator well suited for Hamiltonian systems like FPUT chains [44, 47]. Accordingly, in the present work, the trajectories were generated with high accuracy using a fixed time step of 0.05 [26].

III. A DEEP AUTOENCODER MODEL

The autoencoder is an ANN trained to reconstruct an input vector $\mathbf{x} \in \mathbb{R}^n$ at the output layer, i.e., to produce a reconstruction $\tilde{\mathbf{x}}$, by passing \mathbf{x} through a narrower hidden layer referred to as the latent (or bottleneck) layer. In this layer, the code vector $\mathbf{z} \in \mathbb{R}^m$ ($1 \leq m \ll n$) provides a compressed, low-dimensional, and salient representation of \mathbf{x} . This representation is achieved by minimizing the reconstruction error J_m (see Eq. B3), or equivalently, the mean squared error (MSE) loss. In general, AEs can be regarded as nonlinear generalizations of PCA: indeed, it can be shown that an autoencoder restricted to be linear is equivalent to PCA [48, 49].

In the present work, we shall employ a relatively simple deep autoencoder model with five hidden layers, whose architecture is schematically depicted in the cartoon shown in Fig. 2. The DAE architecture is composed of two sequential networks: the encoder and the decoder. The first maps \mathbf{x} to \mathbf{z} , while the second maps \mathbf{z} to $\tilde{\mathbf{x}}$.

Below, we describe all the model's hyperparameters chosen according to its excellent reconstruction performance of the input data for latent dimension $m \geq 2$ as discussed in Sect. IV. The number of nodes (or neurons) per layer together with the respective activation functions are shown in Table I. Note that all hidden nodes use the popular ReLU (Rectified Linear Unit) activation function, i.e., $h(y) = \max(0, y)$, for learning nonlinear mappings [50]. By contrast, the output layer employs a linear activation function, which is commonly used for regression tasks. However, it would also be possible to choose a linear activation function for the bottleneck layer, since no significant differences in performance are observed.

The model is trained using the Adam optimizer [51] with a default learning rate of 0.001 and a mini-batch size of 256, noting that smaller batch sizes (e.g., 32) do not produce significant differences in performance. The number of training iterations is set to 300 epochs. However, early stopping (ES), which acts as an implicit regularizer with a patience of 30 epochs, is chiefly used to avoid unnecessary training, thereby saving significant time and computational resources. The model is implemented using Keras and TensorFlow [52–54].

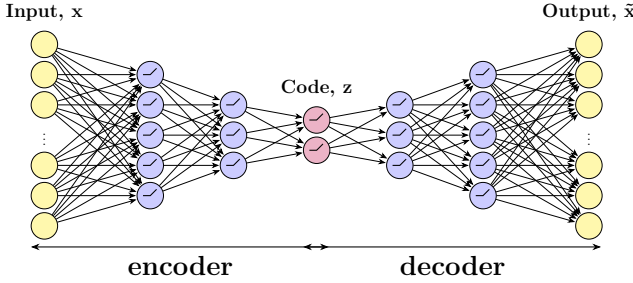


FIG. 2. Schematic view of a DAE model with five hidden layers. The input and output layers contain n nodes, while the bottleneck layer has m nodes ($m \ll n$). All hidden nodes use ReLU activation function, as indicated by the symbol inside the nodes. The output layer's nodes employ a linear activation function which is appropriate for regression.

Layer Type	Nodes	Activation Function
input layer	64	-
encoder layer 1	32	ReLU
encoder layer 2	16	ReLU
hidden layer	m	ReLU
decoder layer 1	16	ReLU
decoder layer 2	32	ReLU
output layer	64	Linear

TABLE I. Number of nodes and respective activation functions of DAE architecture.

In general, especially for neural networks, the training reconstruction error can be very low because the model may fit the training data extremely closely, thereby leading to serious overfitting. As a result, the model may not perform well on unseen data. Accordingly, to ensure that the model generalizes successfully, we split each trajectory dataset into a training set and a test set [55]. The training set contains 70% of the input data, consisting of data points chosen at random, while the test set contains the remaining 30% of the data. Note that 20% of training set is also used as validation set for monitoring the model's generalization during training. With this choice, we find that the difference between the training and test reconstruction errors is generally $\lesssim 10^{-3}$, and decreases to about 10^{-5} for larger bottleneck-layer sizes, i.e., as $m \rightarrow 7$. Overall, these errors are smaller by at least a factor of 100 than the corresponding PCA reconstruction errors. This fact is illustrated for the specific case of $\beta = 1.1$ in the top panel of Fig. 3, where the DAE and PCA reconstruction curves are compared. Therefore, the DAE model provides a significantly more accurate reconstruction of the input data than PCA.

Here, it is worth noting that when the latent dimensionality is restricted to a single variable ($m = 1$), it is unrealistic to expect an autoencoder to capture the complex structure of the 64-dimensional input data, unless the data lie on an approximately one-dimensional manifold [48]. This condition is not satisfied in the present

case, as the intrinsic dimensionality of the trajectory data satisfies ≥ 2 . Consequently, the severe information bottleneck imposed by $m = 1$ leads to underfitting and, therefore, to increased reconstruction errors. Nevertheless, there is no need to modify the present model, as the aforementioned limitation disappears altogether for latent dimension $m > 1$. Instead, we rely on early stopping to retain the model corresponding to the minimum validation error during the optimization of the trainable parameters (weights and biases) [56]. A detailed analysis of the DAE's learning curves for $\beta = 0.3$ is provided in Sect. IV.

A. Datasets and Data Preprocessing

Each dataset of size $n_s = 4\,000\,000$ corresponds to a set $\mathcal{X} = \{\mathbf{x}_1, \mathbf{x}_2, \dots, \mathbf{x}_i, \dots, \mathbf{x}_{n_s}\}$, whose elements $\mathbf{x}_i \in \mathbb{R}^n$ are data points belonging to a single trajectory obtained from numerical simulations of the FPUT system at a given value of $\beta \in [0.1, 1.1]$, sampled at intervals of $\Delta\beta = 0.1$ [21].

The set \mathcal{X} is then conveniently arranged into an $n_s \times n$ data matrix X . However, before feeding it into the DAE model, a data preprocessing step is required, consisting of centering and scaling each variable by its standard deviation, as is customary in PCA [27]. First, centering the data, corresponding to setting the mean of each variable to zero, allows the PCA eigenvalues to be efficiently computed via singular value decomposition (SVD) (see Sect. B). Second, rescaling ensures that each variable, now having unit variance, contributes equally to the analysis regardless of its original scale [27]. This preprocessing step allows for a direct comparison between the DAE results and those obtained from principal component analysis in Ref. [21].

IV. RESULTS AND DISCUSSION

To start with, we briefly analyze the learning curves obtained during model training on trajectory data with $\beta = 0.5$, which exemplify the typical DAE performance across the datasets considered.

In Fig. 3 (main panel), the training and validation mean squared error losses are shown as functions of epoch for bottleneck sizes $m = 1$ and $m = 2$. In both cases, the MSE losses exhibit a rapid initial decay followed by plateau, indicating that the model quickly learns the dominant structure of the data before reaching an error floor, that is, the minimum achievable error. Moreover, for each value of m , the training and validation curves remain close throughout training, suggesting that the DAE generalizes well to unseen data (no overfitting).

However, when the bottleneck dimension is reduced to $m = 1$, the loss saturates at a significantly higher value than for $m = 2$. Specifically, considering that early stopping is triggered at around epoch 116, one finds that the

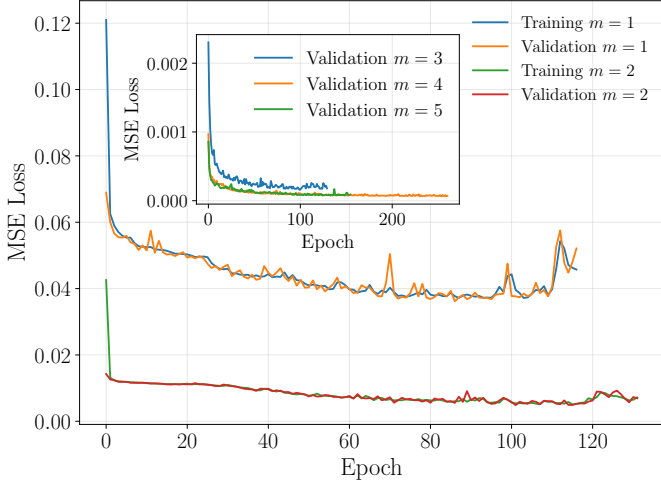


FIG. 3. Training and validation MSE loss curves as functions of epoch for bottleneck sizes $m = 1, 2$ and trajectory data with $\beta = 0.3$. (Inset) Validation MSE loss curves as functions of epoch for $m = 3, 4, 5$ and same data. Throughout training, the deep autoencoder employs an early stopping with a patience of 30.

minimum validation MSE loss ≈ 0.036 which is attained at epoch 86. This is roughly 7 times larger than the corresponding MSE loss observed at $m = 2$ [57]. Additionally, the model's capacity limitation is further evidenced by the noisier evolution of the loss curves for $m = 1$, including the presence of spikes and late-epoch fluctuations. These facts are indicative of optimization difficulties induced by the scalar bottleneck and cannot be substantially mitigated without increasing the latent dimensionality, regardless of changes to the model architecture or hyperparameters, such as the learning rate. By contrast, for $m \geq 2$ the model performs well, yielding substantially smaller reconstruction errors, as further supported by the well-converged validation loss curves for $m = 3, 4, 5$ shown in the inset of Fig. 3.

After training the deep autoencoder, the reconstruction errors J_m obtained from the trained model for a given value β form a curve that depends on the latent dimension m . The intrinsic dimensionality can then be inferred from the elbow of the resulting reconstruction error curve [58]. This heuristic rests on the assumption that, beyond the elbow, J_m no longer decreases significantly as m increases [59]. Note that this approach is inherently subject to a degree of ambiguity and subjectivity, but still routinely employed in machine learning: manifold reduction and clustering [52]. In the following we shall automate the identification of the elbow using the Kneedle algorithm, even though in the present case the elbow points can be easily identified by visual inspection.

In Fig. 4 (top panel), some selected representative reconstruction error curves as functions of m . These curves correspond to $\beta = 0.1, 0.4, 0.7, 0.8, 0.9, 1$, and $\beta = 1.1$. Additionally, a curve from PCA reconstruction error for $\beta = 1.1$ is displayed. It has been rescaled by a factor

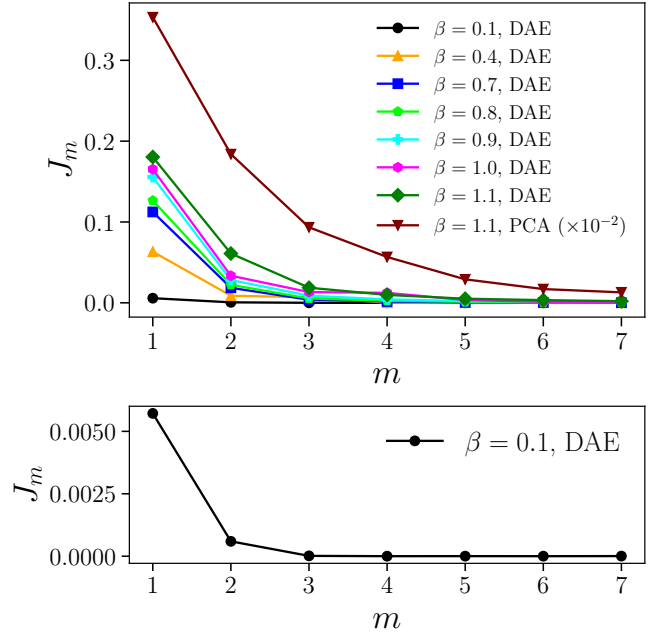


FIG. 4. (Top panel) DAE test reconstruction error curves of the test data as functions of the dimension m for $\beta = 0.1, 0.4, 0.7, 0.8, 0.9, 1.0$, and 1.1 . The PCA reconstruction error curve, corresponding to data with $\beta = 1.1$, is rescaled by a factor of 100 for proper visualization. (Bottom panel) DAE reconstruction error curve for the test data corresponding to $\beta = 0.1$.

of 100 to enable visualization alongside the DAE curves, confirming the superior reconstruction performance of the autoencoder. All DAE reconstruction error curves decrease monotonically, except for the one corresponding to $\beta = 0.1$, whose actual trend is not visible due to its small magnitude. For this reason, this curve is plotted separately in the bottom panel of Fig. 4 to improve visualization. All curves for which $\beta \leq 1$ exhibit an evident elbow point at $m = 2$. Remarkably, this finding agrees with the approach based on multi-chart flows, recently proposed by Yu et al. [37]. By contrast, when $\beta = 1.1$, the elbow point is shifted by unity, as confirmed by the Kneedle algorithm. Therefore, we can conclude that $m^* = 2$ for $\beta \leq 1$, while $m^* = 3$ for $\beta = 1.1$.

We note in passing that one would then expect that a similar approach could be applied straightforwardly to reconstruction error curves at larger values of β . Nevertheless, this is not the case, as for increasing β no evident elbows emerge, similarly to what happens in the linear approach. This fact is addressed in Sect. C, where the DAE and PCA curves correspond to $\beta = 1.8$ (see Fig. 9). Consequently, alternative methods are required to ensure a reliable estimation of ID of trajectory data generated in the strongly nonlinear regime [37, 39, 60].

We can now compare the intrinsic dimensionalities inferred from the DAE with those previously obtained using PCA [21]. Since PCA admits several alternative heuris-

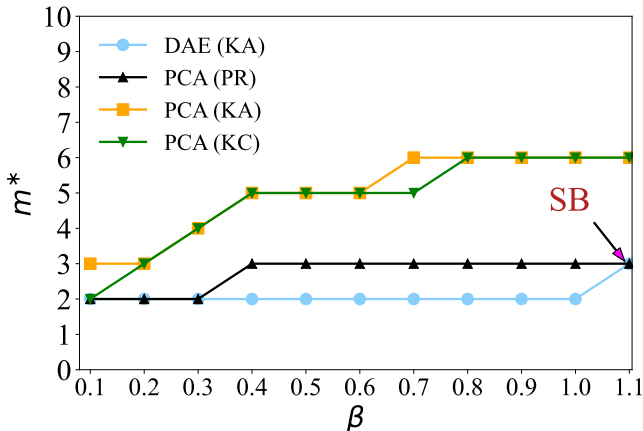


FIG. 5. Estimated intrinsic dimension m^* as function of $\beta \in [0.1, 1.1]$, using DAE model with Kneedle algorithm (KA) and PCA with the following heuristics: Participation Ratio (PR), Kneedle algorithm (KA), and Kaiser criterion (KC).

tics to the Kneedle algorithm, we additionally consider the Kaiser criterion and the Participation Ratio, both of which are computed directly from the PCA eigenvalues (see Sects. B and B1 for details on PCA and for the definitions of the heuristics, respectively).

Fig. 5 clearly shows that PCA combined with KA (squares) and KC (triangles) substantially overestimates the intrinsic dimensionality, especially as β increases, when compared with the DAE results (circles), which instead are consistent with the multi-chart flows approach. By contrast, PCA using PR agrees with the DAE estimates for $\beta \leq 0.3$ and for $\beta = 1.1$, yielding $m^* = 2$ and $m^* = 3$, respectively. We argue that this agreement is purely accidental, since it is well known that PCA tends to overestimate the intrinsic dimensionality when data lie on a nonlinear manifold, as in the present case. A classical example is the synthetic Swiss roll dataset, for which PCA predicts $m^* = 3$, whereas the data actually lie on a two-dimensional manifold ($m^* = 2$) [59, 61].

Additionally, within the linear approach the estimated intrinsic dimensionality remains unchanged as $\beta \rightarrow 1.1$, irrespective of the heuristic used, whereas the DAE predicts an increase to $m^* = 3$.

To understand this dimensionality variation, one needs to consider an important feature characterizing the β model: the symmetry about its center for initially symmetric excitations [19, 62]. This means that if we initially excite a Fourier mode with an odd wave number, then the energy cannot spread to even-numbered modes. In the present case, the initial condition corresponds to assigning the total energy $\mathcal{E}_1 \approx 0.45$ to the first mode E_1 only. As a result, the energy is observed to be shared by odd-numbered modes E_1, E_3 , and E_5 only, in the regime of recurrence, i.e., when $\beta \leq 1$ (see, for instance, Fig. 8).

In contrast, when $\beta = 1.1$, even-numbered modes E_2

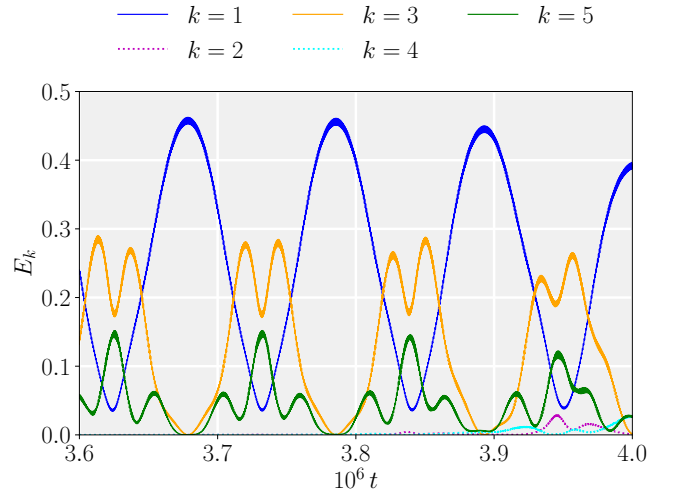


FIG. 6. Time evolution of the energy E_k of the Fourier modes with $k = 1, 2, 3, 4, 5$ in the FPUT β model with $N = 32$ oscillators. The initial condition corresponds to assigning the total energy $\mathcal{E}_1 \approx 0.45$ to the first mode E_1 only.

and E_4 start to be excited. Note that this happens only toward the end of the simulation; see Fig. 6, where E_2 and E_4 can acquire approximately a maximum of 6% of the total energy. Therefore, we can relate the change in ID from $m^* = 2$ to $m^* = 3$ to the occurrence of SB in the β model. We suspect that this variation in ID may imply a substantial difference in the geometric or topological features of the 2-dimensional and 3-dimensional manifolds on which the trajectories lie. Accordingly, this interesting finding could be properly investigated using other ML tools, for instance, those from topological and geometric data analysis [63–69].

One advantage of using autoencoders is the possibility of visualizing the data and thereby gaining meaningful insights into the dynamics. Accordingly, we compute a two-dimensional latent representation (or embedding) of the entire trajectory, consisting of $n_s = 3\,000\,000$ data points, generated at very small nonlinearity, $\beta = 0.1$ [70]. In particular, we compare the two embeddings obtained when ReLU and Linear activation functions are employed in the bottleneck layer. Panels (a) and (b) of Fig. 7 show the resulting two-dimensional embeddings for the ReLU and Linear cases, respectively. In both cases, the embeddings define compact, ring-like regions with sharp, clearly delineated boundaries.

In particular, the embedding in panel (b) confirms that the trajectory data is centered during the preprocessing step. This fact is not evident in the ReLU case, since the activation function clips negative values to zero. Note that the two activation functions yield small, comparable reconstruction errors, i.e., $J_2 \approx 10^{-4}$, confirming that these DAE hyperparameters are essentially equivalent.

Note that the embeddings suggest that the motion is confined in a relatively small region of phase space. As a result, the orbits should lie on a small nonlinear

manifold. In contrast, for larger values of β , for which the system reaches thermal equilibrium, the corresponding two-dimensional embeddings display irregular patterns, suggesting that the trajectory is now free to roam over a much larger region of phase space(unbounded motion). This dynamical behavior is illustrated in Fig. 10, where the data correspond to $\beta = 3$.

V. CONCLUSION

In this work, we addressed the intrinsic dimensionality of high-dimensional trajectories in the FPUT chain using a nonlinear manifold learning approach. To this end, we employed a deep autoencoder model to analyze the trajectory data. Accordingly, we find that in the weakly nonlinear regime ($\beta \lesssim 1$) the orbits lie on a small two-dimensional nonlinear Riemannian manifold. In contrast, a comparison with a linear approach based on principal component analysis shows that it cannot capture the nonlinear structure of the data, thereby yielding questionable results. Additionally, we showed that PCA is unable to detect crucial dynamical changes, such as the symmetry breaking occurring at $\beta = 1.1$. In this case, the autoencoder predicts an increase in the intrinsic dimension by unity, which may be related to significantly different geometric and topological features of the resulting three-dimensional nonlinear manifold.

In future work, it would be highly desirable to validate our findings using alternative approaches that do not rely on heuristics such as the detection of elbow points [37, 39, 60].

Finally, our work shows that a data-driven approach can deliver new and interesting insights into FPUT dynamics, since trajectories exhibit rich geometric features. Furthermore, the use of manifold learning methods, which rests on the *manifold hypothesis*, namely, that high-dimensional data lie near or on low-dimensional manifolds [31, 71], is supported by the applicability of the KAM theorem in the weakly nonlinear regime to β model [6].

ACKNOWLEDGMENTS

The author thank Søren Hauberg for advice on correctly training the deep autoencoder and Alberto Maspero for explaining the Cauchy problem for the FPUT system as a first-order differential system. Most of the code execution for this project was performed using Google Colaboratory. The author is also grateful to Google for supporting this research through the Tensor Research Cloud (TRC) program and for providing access to Cloud Tensor Processing Units (TPUs), which accelerated the machine learning experiments.

DATA AVAILABILITY STATEMENT

The data that support the findings of this study are openly available in Zenodo [72, 73].

Appendix A: FPUT Initial Condition

In the following, we recall how the “half sine” initial condition of FPUT chain is defined a time $t = 0$ [3]. Such a condition corresponds to initially displace the coordinates q_i ($i = 1, \dots, 32$) according to the formula [26]

$$q_i(0) = A \sqrt{\frac{2}{N+1}} \sin\left(\frac{ik\pi}{N+1}\right), \quad (A1)$$

where the amplitude A and wave number k are set to $A = 10$, and $k = 1$, respectively. Note that here $q_0 = q_{N+1} = 0$, that is, the chain’s ends are fixed. Additionally, it is assumed that the variables $p_i(0) = 0$ with $i = 1, \dots, 32$.

Next, the k -th energy (Fourier) mode is defined as [26]

$$E_k = \frac{1}{2} [\dot{a}_k^2 + \omega_k^2 a_k^2], \quad (A2)$$

where $\omega_k = 2 \sin(k\pi/2(N+1))$ is the frequency, a_k denotes the normal mode coordinate ($k = 1, 2, \dots, N$) which reads [26]

$$a_k = \sqrt{\frac{2}{N+1}} \sum_{j=0}^N q_j \sin\left(\frac{jk\pi}{N+1}\right). \quad (A3)$$

Note that this large-wavelength (or equivalently low-frequency) initial condition is equivalent to initially give the total energy $\mathcal{E}_1 \approx 0.45$ to first energy mode E_1 ($k = 1$). In the weakly nonlinear regime ($\beta \lesssim 1$) the recurrence phenomenon occurs. As a result, the total energy is shared by three modes with odd wave numbers $k = 1, 3, 5$, while it cannot spread to modes with even wave numbers due to the parity conservation characterizing the β model [62]. This fact is illustrated in Fig. 8 for $\beta = 1$.

Appendix B: Principal Component Analysis

Let \tilde{X} denote the $n_s \times n$ data matrix, after the data preprocessing, which make the variables scale-free each with zero mean, then the sample covariance matrix (or equivalently correlation matrix) S reads [27]

$$S = \frac{1}{n_s - 1} \tilde{X}^T \tilde{X}. \quad (B1)$$

The eigenvalue λ_i of S correspond to the explained (or preserved) variance along the i -th principal component axis. In present work, the sorted eigenvalues $\lambda_1 \geq \lambda_2 \geq \dots \geq \lambda_i \geq \dots \geq \lambda_n$ are efficiently computed using the singular value decomposition [74, 75]. Accordingly to SVD, $\tilde{X} =$

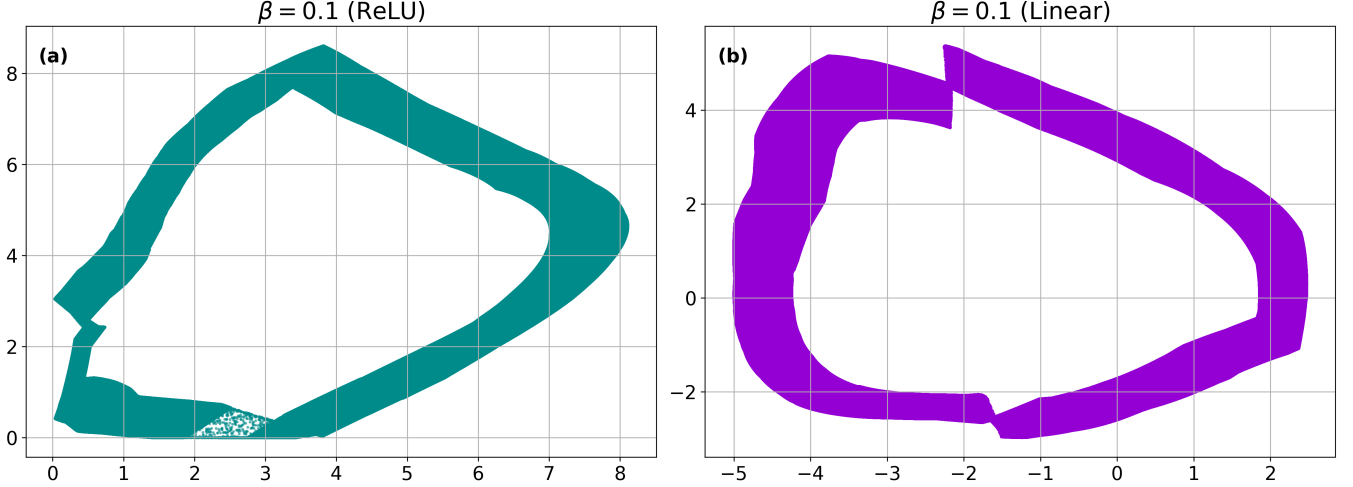


FIG. 7. Two-dimensional DAE embeddings of the entire trajectories comprising $n_s = 3,000,000$ data points corresponding to $\beta = 0.1$. In panels (a) and (b), the embeddings were obtained using ReLU and Linear activation functions in the bottleneck layer, respectively. The reconstruction errors in panels (a) and (b) are the following: $J_2 \approx 6.15 \times 10^{-4}$ and $J_2 \approx 5.91 \times 10^{-4}$ (b), respectively.

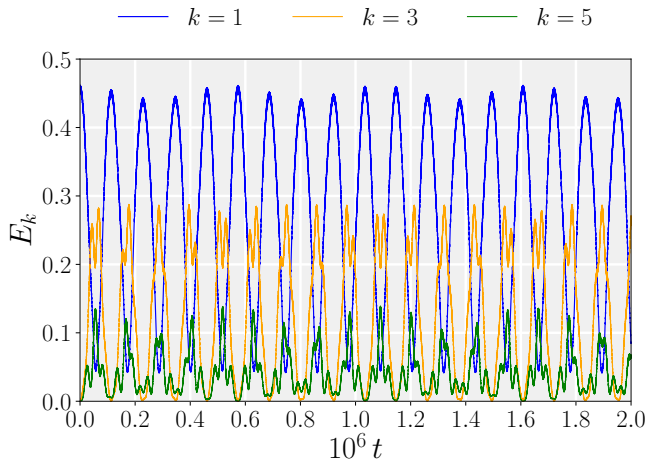


FIG. 8. Recurrence phenomenon. Time evolution of the energy E_k of the Fourier modes with $k = 1, 3, 5$ in the FPUT β model with $N = 32$ coupled oscillators ($\beta = 1$). The initial condition corresponds to assigning the total energy $\mathcal{E}_1 \approx 0.45$ to the first mode E_1 only.

WLV^T where W and V are two orthogonal matrices, and L is a diagonal matrix [27, 30]. As a result, it is found that [27]

$$\lambda_i = \frac{1}{n_s - 1} s_i^2, \quad (B2)$$

where the singular values s_i ($s_1^2 \geq s_2^2 \geq \dots \geq s_n^2 \geq 0$) are the diagonal entries of L , which we computed using scikit-learn library [76].

From the projection perspective PCA orthogonally projects the original data points \mathbf{x}_j onto projected data

points $\tilde{\mathbf{x}}_j$ belonging to a suitable m -dimensional linear subspace (the principal subspace), by minimizing the average reconstruction error J_m which reads [28]

$$J_m = \frac{1}{n_s} \sum_{j=1}^{n_s} \|\mathbf{x}_j - \tilde{\mathbf{x}}_j\|_2^2, \quad (B3)$$

where $\|\cdot\|_2$ stands for the Euclidean norm.

Accordingly, within PCA, Eq. B3 can be rewritten in terms of covariance matrix's eigenvalues λ_i as [77]

$$J_m = \sum_{l=m+1}^n \lambda_l. \quad (B4)$$

It is worth noting here that the eigenvectors relative to the eigenvalues λ_l ($m + 1 \leq l \leq n$) in Eq. B4 constitute the basis of the orthogonal complement of the principal subspace.

Finally, it is worth noting that within PCA, the term PC score vector (or simply scores) replaces the code vector which sits at the AE's bottleneck layer [27].

1. Heuristics for Determining ID in PCA

Determining the intrinsic dimensionality corresponds to find the optimal number of PCs to retain. To this end, there exist various methods. To our best knowledge, the state-of-art method is represented by the Gavish-Donoho optimal hard threshold, which rests on the Marchenko-Pastur distribution [78, 79]. However, this cannot be applied here because the aspect ratio $n/n_s \approx 1.6 \times 10^{-5}$ of \tilde{X} is too small [21].

Jolliffe modified the Kaiser criterion (also known as the Kaiser-Gutman rule) in factor analysis, making it

suitable for PCA [43, 80]. According to Jolliffe's ansatz, the number of principal components which capture most of the variance, corresponds to those PCs for which $\lambda_i \geq 0.7$.

An alternative way to obtain the ID from PCA's eigenvalues is computing the Participation Ratio D_{PR} which estimates the number of dimensions along which the data is distributed [38, 81]. Accordingly, D_{PR} reads [81]

$$D_{\text{PR}} = \frac{\left(\sum_{i=1}^n \lambda_i\right)^2}{\sum_{i=1}^n \lambda_i^2}. \quad (\text{B5})$$

Eq. B5 can be conveniently expressed in terms of the traces of S (Eq. B1) and S^2 , respectively. In such a case, one finds $D_{\text{PR}} = (\text{Tr}(S))^2 / \text{Tr}(S^2)$.

Finally, note that D_{PR} is a real number, so we shall round it to its nearest integer.

Appendix C: Some DAE Results for $\beta = 1.8$ and $\beta = 3$

In Fig. 9, the DAE and PCA reconstruction error curves as functions of the latent dimension m are shown for $\beta = 1.8$. In this case, most DAE computations were performed using Google TPUs; accordingly, the only modification to the autoencoder architecture was an increase

in the batch size from 256 to 512 in order to fully exploit the TPUs. However, this change in the autoencoder's hyperparameters does not affect the overall final result.

Although the curves suggest that the intrinsic dimensionality increases substantially for large β , no clear elbow points are visible, making their identification highly questionable. Accordingly, by applying KA to the DAE reconstruction curve, and PR, KC, and KA to the PCA reconstruction curve, we obtain the estimates $m^* = 6$ for DAE, and $m^* = 6$, $m^* = 17$, and $m^* = 21$ for PCA, respectively.

Assuming, as discussed above, that the PR provides the most reliable estimate of the intrinsic dimensionality in the linear approach, we conclude that both methods predict the same intrinsic dimension, $m^* = 6$, for data with $\beta = 1.8$. Furthermore, DAE aligns with PCA, confirming that the intrinsic dimensionality increases with stronger nonlinearity, as previously reported in Ref. [21].

Next, in Fig. 10, the two-dimensional DAE embedding of the entire trajectory with $n_s = 3000000$ data points and $\beta = 3$ is shown. In contrast to the embeddings obtained for small nonlinearities, i.e., $\beta = 0.1$, there is no longer a well-defined pattern as observed previously. Furthermore, this embedding suggests that the motion is now unbounded, allowing the system to explore a much larger region of the phase space.

For sake of completeness, we report the intrinsic dimensionality of this trajectory data. It is found that PCA estimates $m^* = 10$ (PR), $m^* = 37$, and $m^* = 37$ [21].

- [1] J. Ford and J. Waters, Computer studies of energy sharing and ergodicity for nonlinear oscillator systems, *Journal of Mathematical Physics* **4**, 1293 (1963).
- [2] E. Fermi, J. Pasta, S. Ulam, and M. Tsingou, Studies of nonlinear problems, Los Alamos preprint LA-1940 (1955).
- [3] J. Ford, The fermi-pasta-ulam problem: Paradox turns discovery, *Physics Reports* **213**, 271 (1992).
- [4] T. P. Weissert, *The Genesis of Simulation in Dynamics. Pursuing the Fermi-Pasta-Ulam Problem*, 1st ed. (Springer, New York, NY, 1997).
- [5] G. Gallavotti, *The Fermi-Pasta-Ulam Problem: A Status Report*, Lecture Notes in Physics, Vol. 728 (Springer, Berlin, 2008).
- [6] S. Lepri, R. Livi, and S. Ruffo, 1953: Fermi's "little discovery" and the birth of the numerical experiment, *Giornale di Fisica* **64**, 275289 (2023).
- [7] J. Dongarra and D. Keyes, The co-evolution of computational physics and high-performance computing, *Nature Reviews Physics* **6**, 621 (2024).
- [8] A. N. Kolmogorov, On conservation of conditionally periodic motions for a small change in hamilton's function, *Proceedings of the USSR Academy of Sciences* **98**, 527 (1954).
- [9] V. I. Arnold, Proof of a theorem of kolmogorov on the invariance of quasi-periodic motions under small perturbations of the hamiltonian, *Russian Mathematical Surveys* **18**, 9 (1963).
- [10] J. Möser, On invariant curves of area-preserving mappings

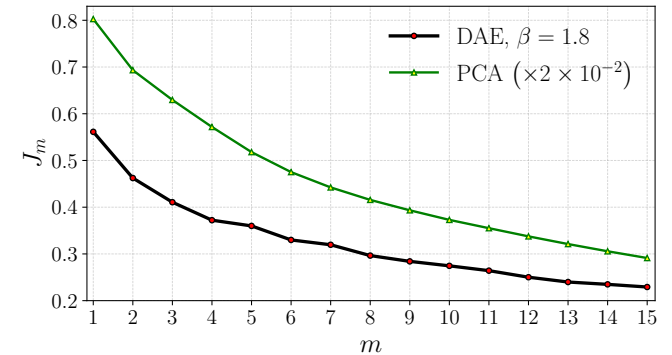


FIG. 9. DAE reconstruction error curve (circle) and PCA reconstruction error curve (triangle), rescaled by a factor of 200, as functions of latent dimension m for trajectory data corresponding to $\beta = 1.8$.

- of an annulus, *Nachr. Akad. Wiss. Göttingen*, II , 1 (1962).
- [11] M. Toda, Vibration of a chain with nonlinear interaction, *Journal of the Physical Society of Japan* **22**, 431 (1967).
- [12] G. Benettin, H. Christodoulidi, and A. Ponno, The fermi-pasta-ulam problem and its underlying integrable dynamics, *Journal of Statistical Physics* **152**, 195 (2013).
- [13] N. J. Zabusky and M. D. Kruskal, Interaction of "solitons"

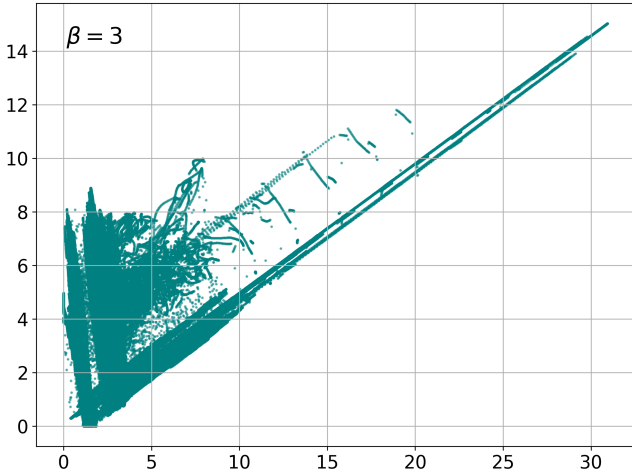


FIG. 10. Two-dimensional DAE embedding of the entire trajectory comprising $n_s = 3000000$ data points for $\beta = 3$. The embedding is obtained using ReLU activation function in the bottleneck layer. In this case, the reconstruction error is $J_2 \approx 0.54$.

in a collisionless plasma and the recurrence of initial states, *Phys. Rev. Lett.* **15**, 240 (1965).

[14] S. Flach, M. V. Ivanchenko, and O. I. Kanakov, q -breathers and the fermi-pasta-ulam problem, *Phys. Rev. Lett.* **95**, 064102 (2005).

[15] S. Flach, M. V. Ivanchenko, and O. I. Kanakov, q -breathers in fermi-pasta-ulam chains: Existence, localization, and stability, *Phys. Rev. E* **73**, 036618 (2006).

[16] F. M. Izrailev and B. V. Chirikov, Statistical properties of a nonlinear string, Soviet Physics Doklady **11**, 30 (1966).

[17] Y. V. Lvov and M. Onorato, Double scaling in the relaxation time in the β -fermi-pasta-ulam-tsingou model, *Phys. Rev. Lett.* **120**, 144301 (2018).

[18] Fucito, F., Marchesoni, F., Marinari, E., Parisi, G., Peliti, L., Ruffo, S., and Vulpiani, A., Approach to equilibrium in a chain of nonlinear oscillators, *J. Phys. France* **43**, 707 (1982).

[19] K. A. Reiss and D. K. Campbell, The metastable state of fermi-pasta-ulam-tsingou models, *Entropy* **25** (2023).

[20] R. Livi, M. Pettini, S. Ruffo, M. Sparpaglione, and A. Vulpiani, Equipartition threshold in nonlinear large hamiltonian systems: The fermi-pasta-ulam model, *Phys. Rev. A* **31**, 1039 (1985).

[21] G. Marchetti, Intrinsic dimensionality of fermi-pasta-ulam-tsingou high-dimensional trajectories through manifold learning: A linear approach, *Chaos: An Interdisciplinary Journal of Nonlinear Science* **35**, 103118 (2025).

[22] K. Huang, *Statistical Mechanics*, 2nd ed. (John Wiley & Sons, New York, 1987).

[23] M. Baldovin, G. Gradenigo, A. Vulpiani, and N. Zanghi, On the foundations of statistical mechanics, *Physics Reports* **1132**, 1 (2025), on the foundations of statistical mechanics.

[24] J. Ford and G. H. Lunsford, Stochastic behavior of resonant nearly linear oscillator systems in the limit of zero nonlinear coupling, *Phys. Rev. A* **1**, 59 (1970).

[25] B. Rink, Symmetric invariant manifolds in the fermipasta-ulam lattice, *Physica D: Nonlinear Phenomena* **175**, 31

(2003).

[26] N. J. Giordano and H. Nakanishi, *Computational Physics*, 2nd ed. (Pearson Prentice Hall, 2006).

[27] I. T. Jolliffe and J. Cadima, Principal component analysis: a review and recent developments, *Philosophical Transactions of the Royal Society A: Mathematical, Physical and Engineering Sciences* **374**, 20150202 (2016).

[28] T. Hastie, R. Tibshirani, and J. Friedman, *The Elements of Statistical Learning*, 12th ed., Springer Series in Statistics (Springer New York Inc., New York, NY, USA, 2017).

[29] J. Lever, M. Krzywinski, and N. Altman, Principal component analysis, *Nature Methods* **14**, 641 (2017).

[30] M. Greenacre, P. J. F. Groenen, T. Hastie, A. I. DEnza, A. I. Markos, and E. Tuzhilina, Principal component analysis, *Nature Reviews Methods Primers* **2** (2022).

[31] M. Meila and H. Zhang, Manifold learning: What, how, and why, *Annual Review of Statistics and Its Application* **11**, 393 (2024).

[32] M. Shinn, Phantom oscillations in principal component analysis, *Proceedings of the National Academy of Sciences* **120**, e2311420120 (2023).

[33] L. van der Maaten and G. Hinton, Visualizing data using t-sne, *Journal of Machine Learning Research* **9**, 2579 (2008).

[34] D. Kobak and P. Berens, The art of using t-sne for single-cell transcriptomics, *Nature Communications* **10**, 5416 (2019).

[35] D. Kobak and G. C. Linderman, Initialization is critical for preserving global data structure in both t-sne and umap, *Nature Biotechnology* **39**, 156 (2021).

[36] C. de Bodt, A. Diaz-Papkovich, M. Bleher, K. Bunte, C. Coupette, S. Damrich, E. F. Sanmartin, F. A. Hamprecht, E. gnes Horvt, D. Kohli, S. Krishnaswamy, J. A. Lee, B. P. F. Lelieveldt, L. McInnes, I. T. Nabney, M. Noichl, P. G. Poliar, B. Rieck, G. Wolf, G. Mishne, and D. Kobak, *Low-dimensional embeddings of high-dimensional data* (2025), arXiv:2508.15929 [cs.LG].

[37] H. Yu, S. Hauberg, M. Hartmann, A. Klami, and G. Arvanitidis, *Learning geometry and topology via multi-chart flows* (2025), arXiv:2505.24665 [cs.LG].

[38] B. Kramer and A. MacKinnon, Localization: theory and experiment, *Reports on Progress in Physics* **56**, 1469 (1993).

[39] K. Zeng, C. E. P. De Jess, A. J. Fox, and M. D. Graham, Autoencoders for discovering manifold dimension and coordinates in data from complex dynamical systems, *Machine Learning: Science and Technology* **5**, 025053 (2024).

[40] I. Goodfellow, Y. Bengio, and A. Courville, *Deep Learning* (MIT Press, Cambridge, MA, 2016).

[41] M. Ranzato, F. J. Huang, Y. Boureau, and Y. LeCun, Unsupervised learning of invariant feature hierarchies with applications to object recognition, in *2007 IEEE Conference on Computer Vision and Pattern Recognition* (2007) pp. 1–8.

[42] V. Satopaa, J. Albrecht, D. Irwin, and B. Raghavan, Finding a "kneedle" in a haystack: Detecting knee points in system behavior, in *2011 31st International Conference on Distributed Computing Systems Workshops* (2011) pp. 166–171.

[43] I. T. Jolliffe, *Principal Component Analysis*, 2nd ed., Springer Series in Statistics (Springer, New York, NY, 2002) pp. XXX, 488, springer Science+Business Media New York; eBook ISBN: 978-0-387-22440-4; Softcover

ISBN: 978-1-4419-2999-0; Published in Springer Book Archive.

[44] G. Benettin and A. Ponno, On the numerical integration of fpu-like systems, *Physica D: Nonlinear Phenomena* **240**, 568 (2011).

[45] The equations of motion are commonly referred to as the canonical Hamilton equations.

[46] A. Maspero, (Private Communication).

[47] E. Hairer, G. Wanner, and C. Lubich, Symplectic integration of hamiltonian systems, in *Geometric Numerical Integration: Structure-Preserving Algorithms for Ordinary Differential Equations* (Springer Berlin Heidelberg, Berlin, Heidelberg, 2006) pp. 179–236.

[48] A. Lindholm, N. Wahlström, F. Lindsten, and T. B. Schn, *Machine Learning: A First Course for Engineers and Scientists* (Cambridge University Press, 2022).

[49] M. Refinetti and S. Goldt, The dynamics of representation learning in shallow, non-linear autoencoders, *Proceedings of the 39th International Conference on Machine Learning*, 18499 (2022).

[50] V. Nair and G. E. Hinton, Rectified linear units improve restricted boltzmann machines, in *Proceedings of the 27th International Conference on Machine Learning (ICML)* (Omnipress, Haifa, Israel, 2010) pp. 807–814.

[51] D. P. Kingma and J. Ba, Adam: A method for stochastic optimization, in *Proceedings of the International Conference on Learning Representations (ICLR)* (2015).

[52] A. Géron, *Hands-On Machine Learning with Scikit-Learn and TensorFlow: Concepts, Tools, and Techniques to Build Intelligent Systems* (O'Reilly, U.S.A, 2019).

[53] F. Chollet, *Deep Learning with Python* (Manning, Shelter Island, NY, USA, 2018).

[54] M. Abadi, P. Barham, J. Chen, Z. Chen, A. Davis, J. Dean, M. Devin, S. Ghemawat, G. Irving, M. Isard, M. Kudlur, J. Levenberg, R. Monga, S. Moore, D. G. Murray, B. Steiner, P. A. Tucker, V. Vasudevan, P. Warden, M. Wicke, Y. Yu, and X. Zhang, Tensorflow: A system for large-scale machine learning, *CoRR abs/1605.08695* (2016), 1605.08695.

[55] S. Hauberg, (Private Communication).

[56] Note that when the model's bottleneck has a single node, i.e., $m = 1$, there are 4,801 trainable parameters.

[57] The best validation MSE loss is ≈ 0.0049 attained at epoch 101 when $m = 2$.

[58] R. B. Cattell, The scree test for the number of factors, *Multivariate Behavioral Research* **1**, 245 (1966).

[59] J. B. Tenenbaum, V. de Silva, and J. C. Langford, A global geometric framework for nonlinear dimensionality reduction, *Science* **290**, 2319 (2000).

[60] Z. Bi and P. L. de Micheaux, *Beyond pca: Manifold dimension estimation via local graph structure* (2025), arXiv:2510.15141 [stat.ML].

[61] S. T. Roweis and L. K. Saul, Nonlinear dimensionality reduction by locally linear embedding, *Science* **290**, 2323 (2000).

[62] S. D. Pace, K. A. Reiss, and D. K. Campbell, The Fermi-Pasta-Ulam-Tsingou recurrence problem, *Chaos: An Interdisciplinary Journal of Nonlinear Science* **29**, 113107 (2019).

[63] G. E. Carlsson, Topology and data, *Bulletin of the American Mathematical Society* **46**, 255 (2009).

[64] F. Chazal and B. Michel, An introduction to topological data analysis: Fundamental and practical aspects for data scientists, *Frontiers in Artificial Intelligence* **4** (2021).

[65] N. Otter, M. A. Porter, U. Tillmann, P. Grindrod, and H. A. Harrington, A roadmap for the computation of persistent homology, *EPJ Data Science* **6**, 17 (2017).

[66] E. Munch, A users guide to topological data analysis, *Journal of Learning Analytics* **4**, 4761 (2017).

[67] M. Papillon, S. Sanborn, J. Mathe, L. Cornelis, A. Bertics, D. Buracas, H. Lillemark, C. Shewmake, F. Din, X. Pennec, and N. Miolane, Beyond euclid: An illustrated guide to modern machine learning with geometric, topological, and algebraic structures, *Machine Learning: Science and Technology* **10.1088/2632-2153/adf375** (2025).

[68] A. Hickok, *Topics in Geometric and Topological Data Analysis*, Phd thesis, University of California, Los Angeles (2023), available at <https://escholarship.org/uc/item/4h6345xq>.

[69] A. Hickok and A. J. Blumberg, *An intrinsic approach to scalar-curvature estimation for point clouds* (2023), arXiv:2308.02615 [stat.ML].

[70] Here we used a smaller number n_s of data points to reduce the computational burden.

[71] C. Fefferman, S. Mitter, and H. Narayanan, Testing the manifold hypothesis, *Journal of the American Mathematical Society* **29**, 983 (2016).

[72] G. Marchetti, Dataset of entire trajectories of fermi-pasta-alam-tsingou model β ($n = 32$, $k = 1$, $a = 10$, $\beta \in [0.1, 1.5]$), [10.5281/zenodo.1585661](https://zenodo.1585661) (2025).

[73] G. Marchetti, Dataset of entire trajectories of fermi-pasta-alam-tsingou model β ($n = 32$, $k = 1$, $a = 10$, $\beta \in [1.6, 3]$), [10.5281/zenodo.15873646](https://zenodo.15873646) (2025).

[74] G. Strang, The fundamental theorem of linear algebra, *The American Mathematical Monthly* **100**, 848 (1993).

[75] G. W. Stewart, On the early history of the singular value decomposition, *SIAM Review* **35**, 551 (1993).

[76] F. Pedregosa, G. Varoquaux, A. Gramfort, V. Michel, B. Thirion, O. Grisel, M. Blondel, P. Prettenhofer, R. Weiss, V. Dubourg, J. Vanderplas, A. Passos, D. Cournapeau, M. Brucher, M. Perrot, and Édouard Duchesnay, Scikit-learn: Machine learning in python, *Journal of Machine Learning Research* **12**, 2825 (2011).

[77] M. P. Deisenroth, A. A. Faisal, and C. S. Ong, *Mathematics for Machine Learning* (Cambridge University Press, 2020).

[78] M. Gavish and D. L. Donoho, The optimal hard threshold for singular values is $4/\sqrt{3}$, *IEEE Transactions on Information Theory* **60**, 5040 (2014).

[79] V. A. Marčenko and L. A. Pastur, Distribution of eigenvalues for some sets of random matrices, *Mathematics of the USSR-Sbornik* **1**, 457 (1967).

[80] H. F. Kaiser, The application of electronic computers to factor analysis, *Educational and Psychological Measurement* **20**, 141 (1960), <https://doi.org/10.1177/001316446002000116>.

[81] S. Recanatesi, S. Bradde, V. Balasubramanian, N. A. Steinmetz, and E. Shea-Brown, A scale-dependent measure of system dimensionality, *Patterns* **3**, 100555 (2022).